HYDRODYNAMIC PERFORMANCE OF A BIOLOGICALLY INSPIRED THREE-DIMENSIONAL FLAPPING FOIL

Alexandra H. Techet ahtechet@mit.edu
Keith L. Lim contact.keithlim@gmail.com
Franz S. Hover hover@mit.edu
Michael S. Triantafyllou mistetri@mit.edu

Center for Ocean Engineering, Department of Mechanical Engineering,
Massachusetts Institute of Technology, Cambridge, Mass.

ABSTRACT—A study of the propulsive properties of a NACA 0012 linearly tapered, rigid foil performing a combined roll and pitch motion are investigated in this paper. A second-generation flapping-foil actuator, equipped with position sensors and a six-axis force sensor was designed for use in a water tunnel facility and is capable of operating in flow with speeds up to 2 m/s. Propulsion tests were performed to measure the mean planform area thrust coefficient and efficiency over a range of frequencies and roll and pitch amplitudes using a six-axis dynamometer. The mean planform area thrust coefficient and efficiency are recorded over a paramtetric space that included three roll amplitudes, with induced heave (at 0.7 span) to chord ratio, $h_{0.7}/c$ = 1.0, 1.5 and 2.0, Strouhal numbers, *St*, ranging from 0.2 to 0.6, and maximum angle of attack varying from 15 to 45 degrees. Results show that a maximum planform area thrust coefficient of 2.09 is achieved at $h_{0.7}/c$ = 1.5, *St* = 0.6 and α_{max} = 30º. The thrust and efficiency contour plots also reveal a useful performance trend where, at low α_{max}, high thrust and efficiency can be gained at sufficiently high Strouhal numbers. A maximum efficiency recorded is about 0.8 at *St* = 0.3 and $\alpha_{max} = 20^{\circ}$ for $h_{0.7}/c$ = 2.0. DPIV is used to study the vortical signature created by the flapping foil. Results show that the vortex patterns are heavily influenced by the foil geometry and kinematics. Vorticity control through the replication of such wake vortex patterns can potentially offer optimal solutions for flapping foil propulsion.

1. INTRODUCTION

Millions of years of evolution have resulted in a vast number of aquatic species with specialized fins geared to produce fast, agile swimmers. These fish and other seagoing animals, such as penguins and turtles, are highly adapted to swimming in the ocean and serve as excellent models for developing novel propulsive devices for underwater vehicles. With the goal of designing compact, agile autonomous and unmanned underwater vehicles (AUVs and UUVs), with low power consumption, engineers have turned to fish and their aquatic counterparts for inspiration. AUVs are being designed with flapping foil propulsors, in lieu of conventional propellers, with the goal of building highly maneuverable AUVs (e.g., [3], [5], [11], [12], [20]). To design such vehicles a comprehensive understanding of the hydrodynamic forces and vortical signature associated with this type of propulsion is essential.

Studies have looked at both live fish swimming and robotic fish-like swimming and flapping foils for further insight. Extensive work by biologists into live fish swimming has been done with a myriad of species (see reviews in [29] and [7]). Investigations aimed at understanding the hydrodynamics of live fish swimming have been performed by researchers such as [2], [6], [14], [19], [23], and [31]. Research with whale fins has shown that leading edge tubercles delay stall and enhance lift [18]; this could prove interesting for flapping foil performance as well.

Researchers have looked at fish-like swimming robots and mechanisms to further elucidate the complex hydrodynamics involved with unsteady swimming (see review in [28]). Flapping foil propulsion has been studied by both engineers and biologists, though predominately from a two-dimensional perspective (see reviews in [24] and [25]). Engineers have investigated the forces and vortical signatures of two-dimensional flapping foils (e.g., [2], [4], [9], [13], [16], [21], and [26]).

Closer look at performance of flapping foils is warranted in order to design vehicles to swim with optimal kinematics: maximizing thrust while optimizing efficiency. This paper presents recent tests with a three dimensional, linearly tapered hydrofoil forced to move in roll and pitching motions. Force data and hydrodynamic efficiencies are presented in comparision with previous tests done by [8], [17], [20], and [21].

2. KINEMATIC PARAMETERS AND DEFINITIONS

2.1 Foil Motion Kinematics

The three-dimensional foil motion is similar to that of a penguin wing or turtle fin. Constrained to move in roll, $\phi(t)$, and pitch, $\theta(t)$, only, a diagram of the motion coordinate system is found in figure 1. The prescribed roll and pitch motions are simple sinusoidal harmonics. The roll motion of the foil is defined as,

$$\phi(t) = \phi_0 \sin(\omega t) \tag{1}$$

where ϕ_0 is the roll amplitude in radians and ω is the frequency of the roll motion in radians per second. The pitch motion of the foil is then defined as,

$$\theta(t) = \theta_0 \sin(\omega t + \psi) + \theta_{bias} \tag{2}$$

where θ_0 is the pitch amplitude in radians and ψ is the phase angle between pitch and roll in radians. When investigating unsteady maneuvering characteristics, the static pitch bias, θ_{bias}, is typically non-zero. For the tests described herein, the pitch bias is set to zero. The phase angle is set to $\pi/2$, as recommended by [21].

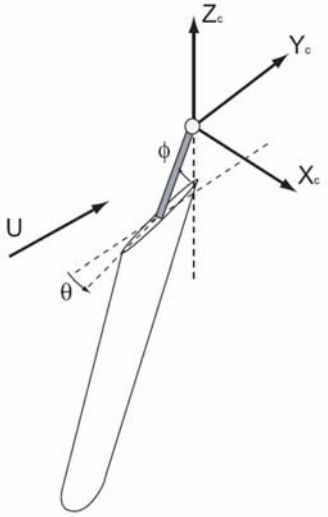

Figure 1: Foil motion coordinate system. The freestream flow is in the Y_c direction and Z_c is oriented in the opposite direction from gravity. Roll, $\phi(t)$, is constrained to the X_c-Z_c plane and pitch, $\theta(t)$, is an angular motion about the foil shaft.

In three-dimensional kinematics, the angle of attack profile varies along the span of the foil as it rolls and pitches. To simplify the three-dimensional kinematics, the motion is decomposed to two-dimensional heaving and pitching at any span location on the foil. The 70% span location (measured from the root of the foil) is taken as the reference position since it is thought that this is close to the effective center of hydrodynamic force. Although [17] results show varying centers of force, the 70% span location is selected to be consistent with conventional propeller notations and for easy comparison with past experiments. This location is defined as

$$r_{0.7} = r_0 + 0.7S\,, \tag{3}$$

where r_0 is the distance from the center of roll axis to the root of the foil, and S is the span of the foil, as seen in figure 2.

The heave position is defined as

$$h(t) = h_0 \sin(\omega t)\,, \tag{4}$$

where h_0 is the amplitude of the heave motion at $r_{0.7}$; h_0 is defined as

$$h_0 = r_{0.7}\phi_0\,. \tag{5}$$

The angle of attack at one span location can be found from the instantaneous pitch position of the foil and the ratio of

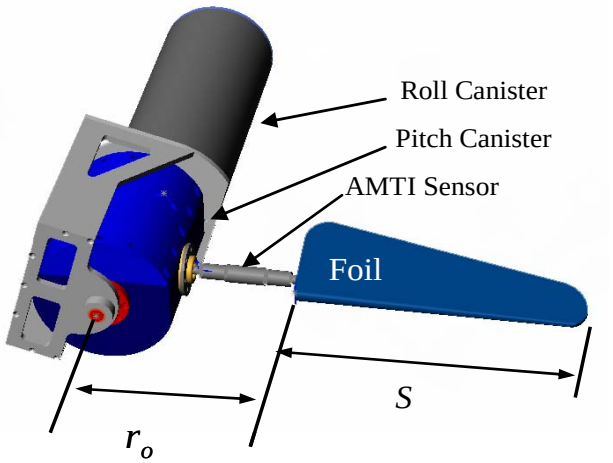

Figure 2: Double canister design with foil attached. AMTI 6-axis force sensor is mounted between the pitch canister and the foil. The distance from center of roll axis to root of foil, r_0.

the heave to forward velocity. Figure 3 shows the vector diagram of the velocity components. A foil with a positive pitch produces a smaller angle of attack and one would need to subtract the angle of attack due to pitch from that due to roll to find the overall angle of attack profile :

$$\alpha(t) = \arctan\left(\frac{\dot{h}(t)}{U}\right) - \theta(t), \qquad (6)$$

where U is the forward speed of the actuator and $\dot{h}$ is the heave velocity. From equation 4, we can express the heave velocity as

$$\dot{h}(t) = \omega r_{0.7}\,\phi_0 \cos(\omega t). \qquad (7)$$

Substituting equation 7 into 6, we get the expression for angle of attack in three dimensional kinematics:

$$\alpha(t) = \arctan\left(\frac{\omega r_{0.7}\phi_0 \cos(\omega t)}{U}\right) - \theta_0 \cos(\omega t) - \theta_{bias}. \qquad (8)$$

The maximum angle of attack achieved is calculated at $r_{0.7}$ and given as $\alpha_{\max} = \max\left[\alpha(t)\right]$ in degrees throughout this paper.

The variation between the actual and the commanded positions are shown in figure 4, where red is the commanded motion and black is the actual motion. Slight variance in the commanded position compared to the actual position resulted from backlash in the system.

2.2 Non-dimensional Parameters

A key parameter used to describe the foil motion kinematics is the Strouhal number, St. Using the same conventions in [27], the Strouhal number is taken as

$$St = \frac{2h_0 f}{U} = \frac{2r_{0.7}\phi_0 f}{U} \qquad (9)$$

where f is the frequency of motion and U is the inflow velocity. An estimate of the total width of the wake produced by the flapping foil is $2h_0$. This is essentially the peak-to-peak amplitude of the foil taken at the 0.7 chord for a 90° phase offset between heave and pitch.

For the three-dimensional case, the roll amplitude is non-dimensionalized by converting this to two-dimensional heave amplitude at 0.7 span and dividing by the chord length, $h_{0.7}/c$. The third parameter used is the maximum angle of attack, in radians, $\alpha_{\max}$. Finally, Reynolds number is calculated based on the chord at 70% of the span.

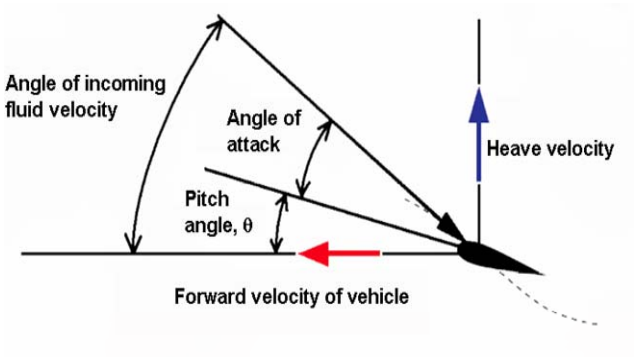

Figure 3: Vector diagram for foil velocity components.

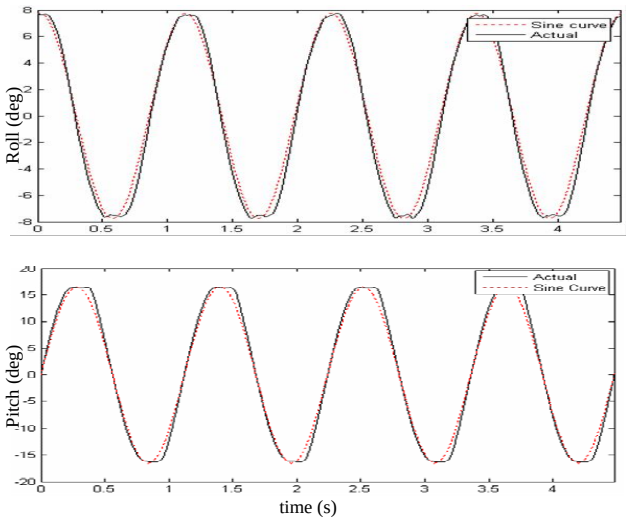

Figure 4: Comparison of actual roll and pitch motions with the commanded motion. Slight variance from commanded position in roll can be attributed to backlash and friction on the rotary shaft seals.

3. EXPERIMENTAL APPARATUS

3.1 Flapping Foil Device

Early flapping propulsion experiments consisted of two-dimensional foils mounted on vertical struts at each end of the foil and motion was provided by chain drive system [26, 21]. To study the effects of three-dimensional foils, it was necessary to design new actuators. In the first generation design, all components and circuitry were located in a single, fixed water-tight housing. Such an actuator was used by [8] her foil experiments. The single housing design simplifies all wiring and mechanical actuation but presents complex sealing problems. Here, a second generation flapping foil actuator was constructed as

a dual canister design. Two watertight canisters, one each for pitch and roll, house only the motor and chain drive for each motion separately. They two canisters are coupled together and to the foil (see figure 2). This apparatus is mounted in the MIT water tunnel as seen in figure 5. All electronic parts are located outside of tunnel. A detailed presentation of the housing design can be found in [15].

To improve force measurements and efficiency calculations, some modifications to the double-housing actuator were made. Two Inscale GL200 hollow-shaft potentiometers were added, one to each of the rotating shafts for position mapping. While the motor encoders provide some indication of pitch and roll angles, these are not reliable indications of the shaft angles over time since some backlash in the chain drive or gear head will cause the shaft rotations to lag that of the motors. Potentiometers mounted directly on the pitch and roll shafts provide accurate feedback on the actual rotations. In addition, an ENTRAN ELT-2 reactive torque sensor was added to the roll motor shaft to measure the power input from the motor end during actuation. This sensor has a torque capacity of 15 Nm and utilizes semi-conductor sensing elements to provide full scale outputs for torque.

For force and torque measurements, the primary sensor used was the AMTI MC1-250, six-axis, water-proof strain gauge sensor. The sensor is basically a six-component transducer, measuring three force components (Fx, Fy, Fz) and three moment components (Mx, My, Mz). Raw time traces of the forces are shown in figure 6. Stainless steel shaft couplings are used to mount the sensor to pitch shaft and foil.

There exists a small percentage of cross-talk between each channel of the sensor which must be accounted for when converting output voltage signals to forces. In the calibration analysis provided by the factory a sensitivity matrix is established to define the 'best fit' linear relationship between all six inputs and corresponding outputs. To verify the sensitivity matrix provided by the factory, a calibration rig was designed to measure the response from all 6 channels. In comparing the diagonals in the matrix against the values provided by AMTI, the error ranged from 0.38% to 3.86%. Since the calibrated results were close to that from AMTI, and the factory calibration technique is more rigorous than the one performed in lab, the factory sensitivity values are used in the computation of forces and moments presented herein. Overall, the factory values represent a more accurate set of calibration since they were evaluated using ten mass points per channel which extend up to the load capacity of the respective channels.

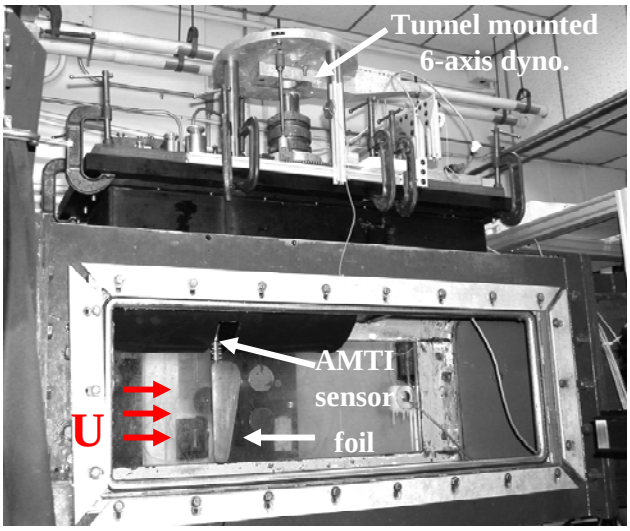

Figure 5: MHL water tunnel facility. The foil actuator is housed within an anodized Aluminum housing on top of which, sits the tunnel dynamometer. The actuator is held in place by a shaft from the C-bracket to the collar of the dynamometer. When assembled, there is a separation distance of about 1cm between the bracket and the dynamometer window. C-clamps are then used to attach the dynamometer window to the housing.

The forces and moments signals from the MC1 sensor were recorded by a custom built National Instrument's Labview software interface and saved for post-processing in Matlab. Raw data traces are shown in figure 6; post-processed force data traces are shown in figure 7. The average thrust and lift forces were found by applying the force rotation matrices and averaging the data over 10-15 cycles. Mean force data presented in subsequent sections are given in terms of the non-dimensional force coefficient, based on the planform area of the foil instead of the swept area as would be used for a propeller. The hydrodynamic efficiency was then measured by comparing the power output, determined from the product of average thrust and velocity, to the sum of the power input applied to the pitch and roll axes. This data is presented in § 4.

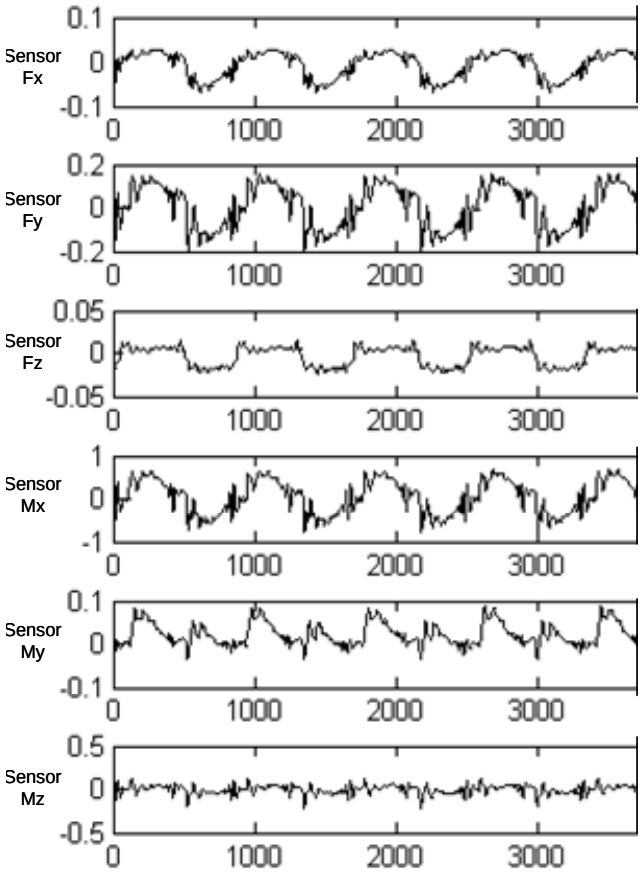

Figure 6: Raw data recorded at St = 0.2 , $h_{0.7}/c$ = 1.5, and α_{max} = 20º. Signals are in voltages and the horizontal axis shows the sample points (N samples). Sampling rate is at 500 Hz. The six plots show voltage signals from the MC1 sensor: three force components and three moments.

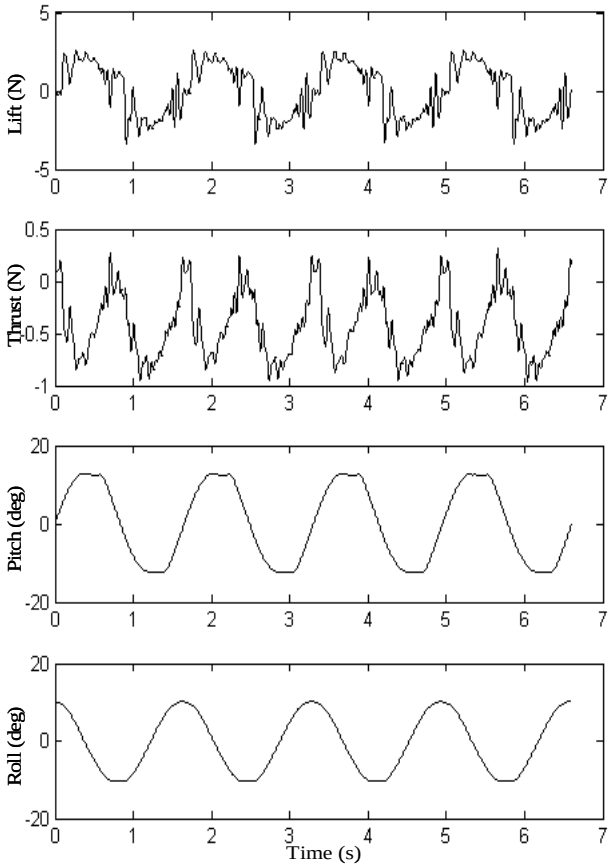

Figure 7: Processed data recorded St = 0.2, $h_{0.7}/c$ = 1.5, α_{max} = 20º. The horizontal axis is the time, in seconds. The lift and thrust are in the tunnel reference frame. The forces are computed using the MC1 sensor measurements taken from the data set as shown in figure 6 and calibrated using the AMTI sensitivity matrix.

3.2 Range of Kinematic Parameters

The foil used in this experiment is identical to the one used by [17]. It features a NACA 0012 cross section, with a span of 24.6 cm and 5.5 cm average chord length. The foil has a linearly tapering trailing edge profile as shown in Figure 2. This foil was cast from a mold using low viscosity urethane forming a rigid wing structure. A stainless steel triangular frame was inserted to the foil for added rigidity. The skeletal frame terminates with a 3/8 in diameter rod extending from the root to allow connection to the shaft coupling. Kinematic parameters used were based on the 0.7 chord length.

Tests were performed over a ranger of kinematic parameters:

- Heave/Chord ratio: $h_{0.7}/c$ = 1.00:0.5:2.00
- Strouhal number: St = 0.2:0.1:0.6
- Maximum AOA: α_{max} = 15:5:45º

The boundary of parametric space represents the mechanical limits of the actuator. Heave/chord ratio is bounded by the maximum roll possible before tunnel side wall effects are significant. The actuator was operable for oscillations of up to 1.5 Hz, beyond which the actuator stalls. Further fine-tuning of the PID limits would have been necessary to achieve higher oscillation frequencies. The lower bound of the parametric space is also the point at which the angle of attack profiles start corrupt (thus producing drag). Force data at higher Strouhal numbers and AOA have been well mapped out by [8] and [20]. [17]

began to investigate regimes of low Strouhal numbers and AOA but experienced appreciable errors due to difficulties in estimating pitch position and velocities.

The experiments were conducted mainly at inflow speeds of 0.5 m/s and 1.0 m/s. The lower speed was used to achieve higher Strouhal numbers. The speed was monitored at all times by a Laser Doppler Velocimetry (LDV) system and maintained to within $\pm$ 0.01 m/s.

4. RESULTS

4.1 Thrust Measurements

The average thrust is calculated by

$$\bar{F}_{x_0} = \frac{1}{T}\int_0^T F_{x_0}(t)dt\,, \qquad (10)$$

such that $\bar{F}_{x_0}$ is the x-force component translated into the reference frame of the tunnel, averaged over one flapping cycle. By axes convention, x is positive upstream. The thrust coefficient is thus defined as

$$C_T = \frac{-2\bar{F}_{x_0}}{\rho U^2 \bar{c}\, S} \qquad (11)$$

where U is the flow velocity, S is the span and $\bar{c}$ is the average chord length. Tables 1 to 3 show the results for C_T for three different roll amplitudes, with induced two-dimensional heave to chord ratio, $h_{0.7}/c$ of 1.0, 1.5 and 2.0, respectively; angle of attack is given in degrees (º).

$\alpha_{\max}$	St			
	0.2	**0.3**	**0.4**	**0.5**
45				1.296
40			0.434	1.374
35		0.294	0.696	1.457
30		0.399	0.736	1.533
25	0.128	0.452	0.918	1.487
20	0.195	0.436	0.974	1.397
15	0.209	0.391	0.869	

Table 1: Results of C_T, for $h_{0.7}/c$ =1.0, from St = 0.2 to 0.5 and $\alpha_{\max}$ = 15° to 45°.

$\alpha_{\max}$	St				
	0.2	**0.3**	**0.4**	**0.5**	**0.6**
45				0.824	1.901
40			0.633	1.014	2.006
35		0.360	0.734	1.143	2.043
30		0.509	0.735	1.403	2.093
25	0.184	0.527	0.777	1.374	1.760
20	0.200	0.599	0.695	1.260	1.489
15	0.241	0.444	0.552	0.720	

Table 2: Results of C_T, for $h_{0.7}/c$ =1.5, from St = 0.2 to 0.6 and $\alpha_{\max}$ = 15° to 45°.

$\alpha_{\max}$	St				
	0.2	**0.3**	**0.4**	**0.5**	**0.6**
45				0.895	1.457
40			0.602	1.095	1.673
35			0.719	1.220	1.747
30			0.872	1.311	1.783
25	0.226	0.385	0.866	1.312	1.660
20	0.159	0.463	0.708	1.065	0.990
15	0.233	0.450	0.549	0.705	

Table 3: Results of C_T, for $h_{0.7}/c$ =2.0, from St = 0.2 to 0.6 and $\alpha_{\max}$ = 15° to 45°.

The general trend of the results compares well with those of [21] (for the 2-dimensional case) and [17] (for the 3D case.) In general, the thrust coefficients are the lowest at lower Strouhal numbers and $\alpha_{\max}$ values. The coefficient starts to increase with increasing values of both Strouhal number and $\alpha_{\max}$. For the case of $h_{0.7}/c$ = 1.0, a peak thrust coefficient of 1.6 was recorded for St = 0.5 and $\alpha_{\max}$ = 30°. Projecting up to $St = 0.6$, it appears that a higher peak thrust coefficient could be achieved; data from [17] substantiates this projection.

For the case of $h_{0.7}/c$ = 1.5, a peak thrust coefficients were measured for St = 0.6 and angle of attacks of 30° and 35°. At $h_{0.7}/c$ = 2.0, the maximum thrust coefficients now occur at the same Strouhal numbers ($St = 0.6$) but have lower magnitudes at $\alpha_{\max}$ = 30° and 35°. Comparisons with two-dimensional cases show similar trends. [21] measured a peak thrust coefficient of 2.17 for a high aspect ratio, 2D flapping foil. The maximum thrust coefficient recorded by [17] was 2.2 at $h_{0.7}/c$ = 1.5.

Using contour plots, it can be seen that, for a given Strouhal number (figures 8 and 9 top plot), the thrust coefficient increases with the maximum angle of attack. However beyond a critical α_{max} value, the thrust coefficient will start to decrease. A similar trend is seen in terms of thrust dependency on roll amplitudes. The maximum thrust coefficient is recorded at $h_{0.7}/c$ of 1.5. At a higher roll amplitude ($h_{0.7}/c$ = 2.0), the peak thrust coefficient is lower. It is possible that an optimal roll amplitude can be found (between the heave to chord ratio of 1.5 to 2.0) for which the thrust coefficient can be maximized.

The left and bottom 'borders' of the parametric space represent the boundaries for which the angle of attack profiles tend to corrupt, that is, some regions of the foil would encounter negative angles of attack, resulting in drag instead of thrust production. Here, the results at St = 0.2 show very low thrust production for all α_{max} values. This low thrust boundary represent the transition in the wake from drag to thrust producing vortices [8]. At high α_{max}, the transition to thrust does not occur until a Strouhal number of about 0.4.

It must be noted that at the experimental points for which low thrust values were measured ($St \leq 0.3$, $15^o \leq \alpha_{max} \leq 25^o$), there are large errors associated with the results. Hence there are some inconsistencies in the trend relating C_T to variations in α_{max}. A more thorough analysis of the error is given in § 4.3.

The thrust coefficients presented above were evaluated based on planform area. A more appropriate normalization, in keeping with that used in propeller performance analysis, would have been to use the projected swept area. This formulation would have produced numerically smaller results (see table 8).

4.2 Hydrodynamic Efficiency

The hydrodynamic efficiency of the foil is defined as the ratio of power output over power input:

$$\eta = \frac{P_{out}}{P_{in}}, \qquad (12)$$

where the power output is the product of the time-averaged thrust and flow velocity

$$P_{out} = TU = -\bar{F}_{x_0} U. \qquad (13)$$

Here, P_{in} is the power input to the fluid, measured by the MC1 sensor mounted to the foil shaft. While the torque sensor attached to the roll motor could measure the direct power input from the electric motor, a large amount of the power is actually used to move the inertial mass of the pitch canister. The motor power input is found to be in the order of ten greater than the power transmitted to the flow. Thus, using the power input from the motor would result in the overall efficiency of the actuator being significantly reduced. This information would then be motor-specific and is then useful only in power system design applications using similar motors. Hence, a more useful approach was to use the power input measured by the MC1 sensor to calculate hydrodynamic efficiency of the foil. This way, the hydrodynamic efficiency of the foil can then be compared directly with other foil designs in future. The hydrodynamic efficiencies from the propulsion experiments are presented in tables 4 to 6.

α_{max}	St			
	0.2	**0.3**	**0.4**	**0.5**
45				0.251
40			0.136	0.295
35		0.231	0.243	0.343
30		0.351	0.288	0.424
25	0.254	0.478	0.418	0.483
20	0.493	0.565	0.535	0.54
15	0.703	0.653	0.614	

Table 4: Efficiency, η, of foil flapping at $h_{0.7}/c$ = 1.0

α_{max}	St				
	0.2	**0.3**	**0.4**	**0.5**	**0.6**
45				0.190	0.269
40			0.246	0.251	0.315
35		0.276	0.321	0.311	0.358
30		0.426	0.361	0.427	0.463
25	0.378	0.52	0.479	0.507	0.456
20	0.513	0.828	0.536	0.614	0.578
15	0.803	0.788	0.599	0.603	

Table 5: Efficiency, η, of foil flapping at $h_{0.7}/c$ = 1.5

α_{max}	St				
	0.2	**0.3**	**0.4**	**0.5**	**0.6**
45				0.202	0.229
40			0.238	0.27	0.279
35			0.32	0.352	0.336
30			0.448	0.429	0.402
25	0.153	0.328	0.54	0.518	0.489
20	0.361	0.473	0.553	0.604	0.498
15	0.802	0.593	0.647	0.658	

Table 6: Efficiency, η, of foil flapping at $h_{0.7}/c$ = 2.0

In a reverse fashion to the C_T results, the efficiency peaks at the lower end (at low Strouhal and α_{max} values) and then decreases with increasing St and α_{max} values. This is as expected since, at the low thrust regions, little energy is lost through kinetic energy being imparted to the flow. The maximum efficiency recorded is about 0.8 at St = 0.3 and α_{max} = 20º for $h_{0.7}/c$ = 2.0. Its location corresponds with that from [17], although numerically the peak values differ. It is noted that his values at this low thrust regime were susceptible to high percentage errors. [21] also shares the same peak location with measured efficiencies not exceeding 0.7.

Higher roll amplitudes result in greater energy expended in moving the foil through the large oscillations. It is only at higher frequencies where greater thrust is generated such that the efficiency appears to be improving. Following this trend, the efficiency data is compared with the corresponding C_T plots in figures 8 and 9.

Here, results show that for low α_{max} values, thrust generally increases with Strouhal number, without much penalty to efficiency. This would be of much interest to power systems design as an optimal point can be identified for relatively high thrust production with good efficiencies. For example, at $h_{0.7}/c$ of 1.5, we see relatively high efficiencies occurring at St = 0.5, and α_{max} of 15º and 20º. This offers a good design point where efficiencies of more than 0.6 can be achieved with thrust coefficients ranging from 0.7 to 1.2. It must be noted that at the low thrust regimes ($St \leq 0.3$, $15º \leq \alpha_{max} \leq 25º$), the percentage errors associated with the measurements remain significant.

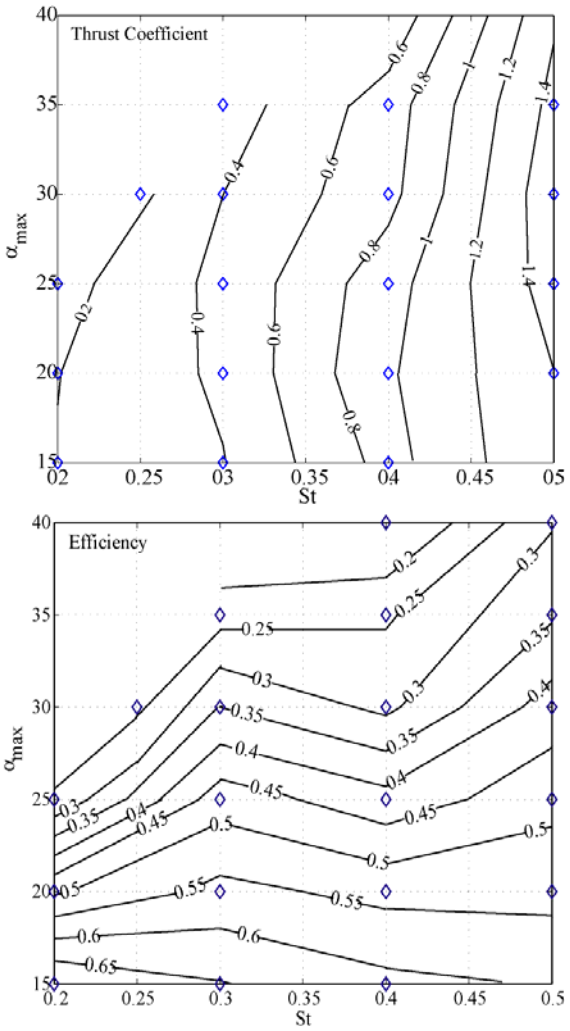

Figure 8: Contour plots of thrust coefficient and efficiency for h_o/c = 1.0. α_{max} is given in degrees (º).

4.3 Repeatability and Error Analysis

To evaluate the repeatability of the results, four sets of five repeated runs were performed. Test cases where large experimental errors could be expected were selected. In this case, runs were done at experimental points where low thrust values were found. Also, cases where there were reasonable thrust and efficiency were repeated to verify the results. The standard deviation for each set was evaluated and the error expressed as the percentage of the standard deviation from the mean. To have a sense for the precision of the MC1 six-axes sensor, the range was also determined. This is taken as the average of the difference between the highest and lowest sample from the mean. The results are presented in Tables 4-8 below.

The average range of C_T is found to be in the order of ± 0.026, or ± 0.044 N in terms of absolute thrust. In other words, the sensor exhibits a precision of about ± 0.044 N. As such, the percentage error, which is taken as the fraction of standard deviation over the mean, is naturally higher at the lower thrust runs (Cases I and III). Likewise a larger percentage error for η arises for Cases I and III.

In all cases, the measured efficiency is 0.6 and above. Hence, while percentage errors appear to be tolerable (about 4-9 %, with the exception of Case IV), the absolute error range is large. This error range would be less than ideal for the low efficiency runs. Since the thrust is used directly in the computation of power output, the error gets transferred to the efficiency calculations. The error for η is thus a combination of errors from power input and thrust measurements. The data is, however, inconclusive in determining which error contribution is more dominant in influencing the efficiency results.

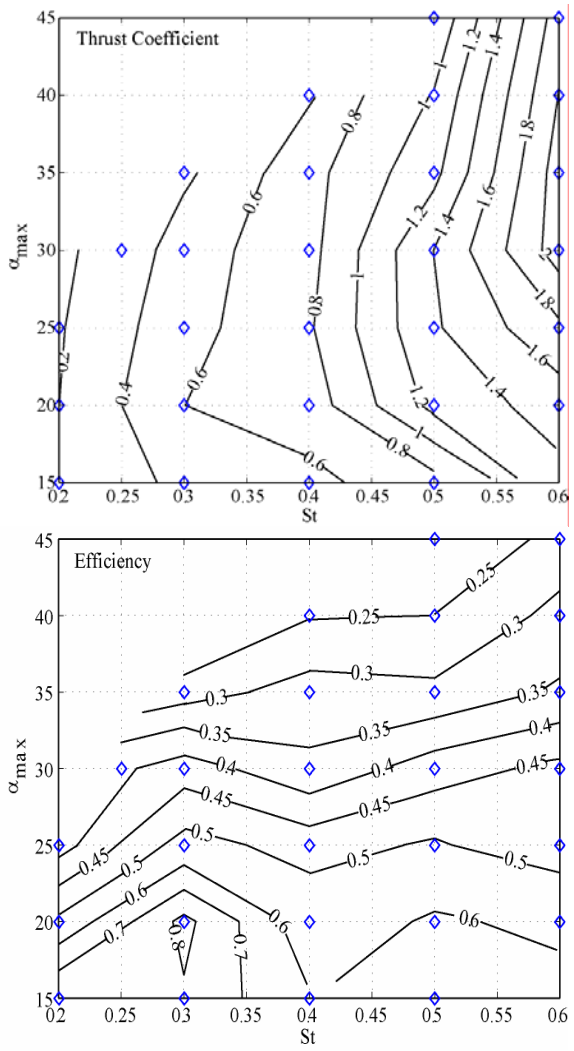

Figure 9: Contour plots of thrust coefficient and efficiency for h_o/c = 1.5. α_{max} is given in degrees (º).

Case I	$h_{0.7}$ / c = 1.0, St = 0.2, α_{max} = 15º			
		C_T	P_{in}	η
	Mean	0.2088	0.2515	0.7031
	Std dev	0.0158	0.0101	0.0589
	% Error	7.5787	4.0280	8.3726
	Range (±)	0.0221	0.0137	0.0715
Case II	$h_{0.7}$ / c = 1.5, St = 0.3, α_{max} = 20º			
		C_T	P_{in}	η
	Mean	0.5995	0.6122	0.8284
	Std dev	0.0216	0.0124	0.0339
	% Error	3.6041	2.0322	4.0874
	Range (±)	0.0291	0.0196	0.0940
Case III	$h_{0.7}$ / c = 2.0, St = 0.2, α_{max} = 15º			
		C_T	P_{in}	η
	Mean	0.2333	0.2459	0.8024
	Std dev	0.0212	0.0031	0.0698
	% Error	9.0670	1.2462	8.7001
	Range (±)	0.0245	0.0047	0.0794
Case IV	$h_{0.7}$ / c = 2.0, St = 0.5, α_{max} = 20º			
		C_T	P_{in}	η
	Mean	1.0645	1.4908	0.6040
	Std dev	0.0234	0.0435	0.0082
	% Error	2.1941	2.9204	1.3536
	Range (±)	0.0283	0.0639	0.0123

Table 7 : Error analysis for repeat runs

Cases II and IV show promising results in terms of identifying design points with combinations of relatively high thrust with good efficiencies. It should be noted, though, that the high thrust coefficients are artificially high since planform area was used to normalize the forces. A more useful normalization would be to use the swept area, which, in this case, is function of both the roll and pitch amplitudes and the distance between the foil and the roll axis of rotation.

To avoid complicated geometrical calculations, an approximation using just the roll amplitude, ϕ_0 is applied. Considering the foil has a zero degree pitch angle at both extremes of the roll motions, the swept area is approximated by

$$SA = 2\phi_0\left[\left(R_0 + S\right)^2 - R_0^2\right], \qquad (14)$$

where R_0 is the distance from center of rotation to the root of the foil and S is the span of the foil. Hence the thrust coefficient would be defined by

$$C_{T_{SA}} = \frac{\bar{F}_{x_0}}{\frac{1}{4}\rho\phi_0 U^2\left[\left(R_0+S\right)^2 - R_0^2\right]}. \qquad (15)$$

By this definition, the effective thrust coefficient is significantly smaller. Table 8 presents the newly calculated values for C_T for cases II and IV. As an additional check, the ideal efficiency (based on actuator disc theory) was computed using the swept area thrust coefficient. Not surprising, the measured efficiency is found to be lower than the ideal efficiency, which serves as the upper bound for conventional propulsors.

Cases	Planform C_T	Swept Area C_T	Measured η	Ideal η
II	0.5995	0.1118	0.828	0.974
IV	1.064	0.1493	0.604	0.965

Table 8: Coefficients of thrust based on swept area

Next, to show repeatability, the force and position time traces for each repeat run were plotted over each other for comparison. For clarity, only three runs for a particular test case are plotted over each other. Figures 10 and 11 show the runs from Case I and Case IV respectively, where the lift force (show in the roll reference frame), drag force, pitch and roll are plotted. These cases correspond to one with large percentage errors (Case I) and another where small percentage errors were calculated (Case IV).

For both of these cases, the data overlapped reasonably well for all measurements. The multiple runs for Case IV were in better agreement. For Case I, it would seem that there was a slight variation in the roll motion for each run, either in magnitude or in phase, which might have accounted for the variations in results. This is less obvious for Case IV due to the scaling of the plots for larger amplitudes.

Small perturbations were observed in the roll plots. Visual checks showed that the roll motion was physically stable. Instead, the roll potentiometer seemed to be picking up some intermittent electromagnetic interference. Fortunately, the noise was only present in this last stage of the tests; the quality of the earlier runs remains intact.

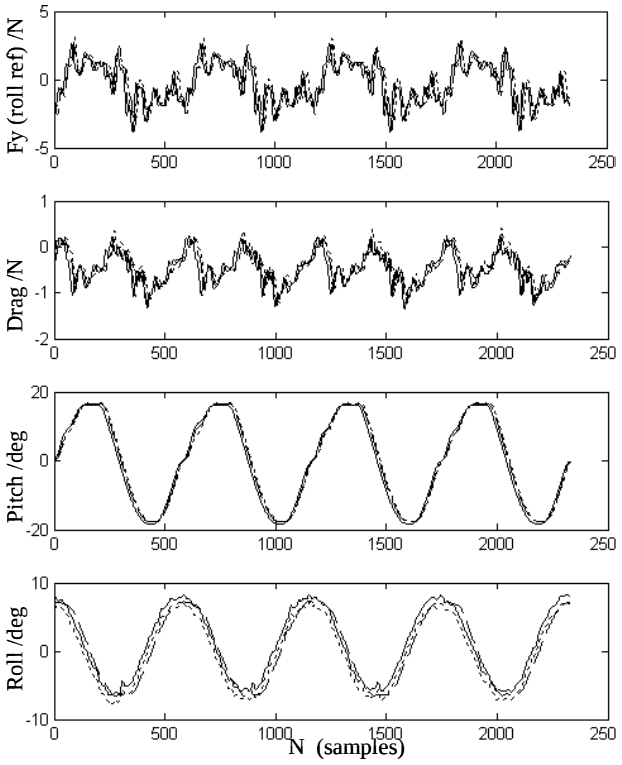

Figure 10: Tests for repeatability show three separate runs for St = 0.2, $h_{0.7}/c$ = 1.0, α_{max} = 15º. Case I.

Overall, the drag force oscillated below the zero mean, hence producing a net thrust. At the same time, its frequency is twice that of the lift. This is because thrust is produced on both the positive and negative stroke of the roll motion.

The recorded pitch motion is fairly sinusoidal. Some backlash appears to occur at the maxima of the pitch motion, causing the peaks to plateau slightly. A slight kink, observed in every upcrossings of the pitch time trace, can be attributed to the 'grabbing'effect due to friction the pitch shaft seal.

4.4 DPIV Results

To further understand the performance of the three-dimensional flapping foil, quantitative flow measurements were taken in the wake to observe the vortical structures generated by the foil. Two-dimensional cuts through the wake were visualized using particle image velocimetry (PIV). The fundamentals of PIV can be found in [1] and [30]. The system used in these experiments was comprised of a New Wave Gemini PIV laser (120mJ/pulse, 15Hz @ 532 nm) and a Kodak/Redlake 4.2MPix camera with a maximum frame rate of 15Hz.

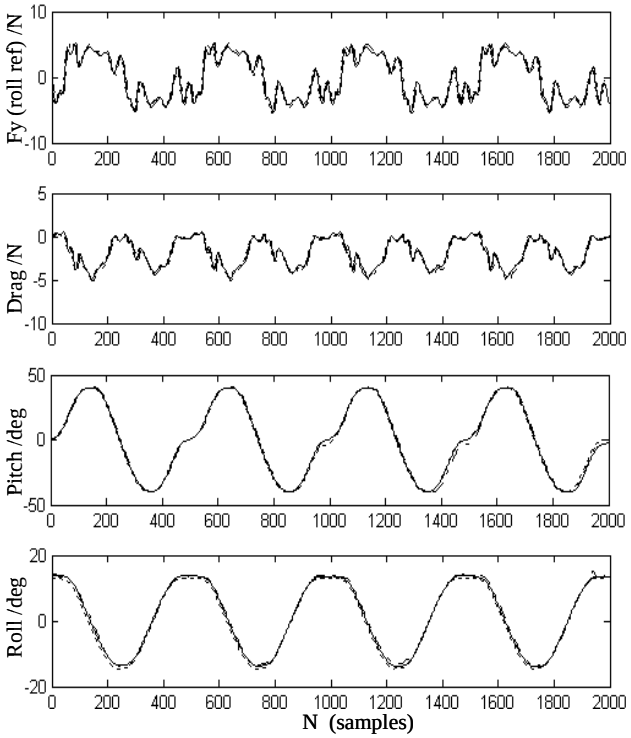

Figure 11: Tests for repeatability show three separate runs for case St = 0.5, $h_{0.7}/c$ = 2.0, α_{max} = 20º. Case IV.

Test Case	Flow Parameters*
1	St = 0.2, $h_{0.7}/c$ = 1.5, α_{max} = 15º
2	St = 0.2, $h_{0.7}/c$ = 1.5, α_{max} = 25º
3	St = 0.5, $h_{0.7}/c$ = 1.5, α_{max} = 25º
4	St = 0.5, $h_{0.7}/c$ = 2.0, α_{max} = 20º

*based on 0.7 span location

Table 9: DPIV test cases to examine effects of St and α_{max} on wake formation.

The data acquisition was synched with the foil motion to obtain phase averaged data. Images were processed using the LaVision DaVis software package and post-processed using MATLAB.

A total of four experimental points were examined with DPIV, at two different planes of view, demarcated by the foil span positions. The first view plane, cut A, was captured at mid-span, with local chord length, $c_{0.5}$ = 58.7 mm. The second plane, cut B, was taken at 0.8 span ($c_{0.8}$ = 43.6 mm). The experimental points were chosen to examine effects of *St* and α_{max} on the wake structure formation. It is also an attempt to capture the flow at different regimes of low or high thrust/efficiencies. The global (0.7 span) parameters corresponding to the cases investigated using DPIV are tabulated in Table 9.

To have an appreciation for the expected wake patterns from the experiments, the experimental points were mapped against the vortex pattern map (as shown in Figure 12) developed by Anderson [2] for the two-dimensional flapping foil case. This plot maps how the wake vortical patterns vary with the flow parameters. Since the foil used in our experiment is three-dimensional (non-uniform tapering geometry) the patterns could vary along the span. Thus the equivalent two-dimensional flow parameters at mid- and 0.8 span locations were considered. These localized parameters are presented in Table 10.

Case		Pos	*St* local	α_{max} local	C_T	η	Legend
1	A	0.5	0.18	12.1º	0.24 (low)	0.803 (high)	
	B	0.8	0.21	16.3º			
2	A	0.5	0.18	22.1º	0.18 (low)	0.378 (low)	
	B	0.8	0.21	26.3º			
3	A	0.5	0.44	21.7º	1.37 (med.)	0.507 (med.)	
	B	0.8	0.52	26.3º			
4	A	0.5	0.45	16.8º	1.18 (med.)	0.62 (high)	
	B	0.8	0.53	21.5º			

Table 10: Local flow parameters for the two spanwise positions where DPIV was performed.

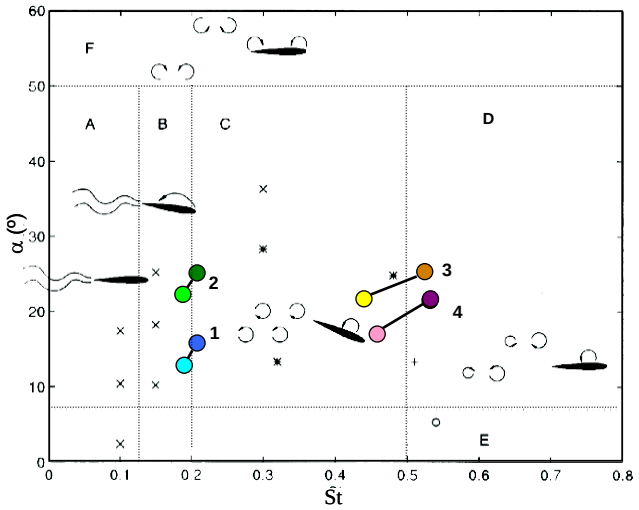

Figure 12: Map of shedding patterns for 2D flapping foils from [2], with local parameters, taken from table 10, for tapered 3D flapping foil superimposed.

Anderson's vortex pattern map (figure 12) depicting the patterns formed in a two-dimensional flapping foil on a plot of Strouhal number against angle of attack. She demarcated six different wake regions in this map as follows:

A. A loosely organized Kármán street along the path of the trailing edge.
B. A Kármán steet forms as in A, but in addition, a sluggishly organized leading edge vortex is evident, even at low angles of attack.
C. Two leading edge vortices are shed per cycle forming a jet wake.
D. Four vortices are shed per cycle, two originating from the leading edge and two from the trailing edge.
E. Four vortices are shed which all originate from the trailing edge.
F. The 'piston mode' shedding characterized by very high angle of attack. A mixed wake is produced by shedding from both edges.

Anderson concluded that the shape of the angle of attack profile significantly influenced the wake structure. This profile is generally harmonic but flattens out as Strouhal number is increased. Sinusoids and square wave profiles produced the clearest wakes. She also observed that multiple peaks in the angle of attack profile at high Strouhal number caused additional shedding that mixes the wake.

In the PIV experiments performed here, at low Strouhal numbers and $\alpha_{\max}$, shear layer vortices are typically seen as the dominate flow structure. At higher Strouhal numbers, coherent vortices are seen being shed into the wake either singly or in pairs. The LE vortex either merges with the TE vortex and convects downstream as a single vortex or in some cases, mixed pairs of opposite sign exist to produce strong thrust.

For Cases 1 and 2 where the thrust production is low, only shear layer vortices were visible. The PIV data showed no evidence of coherent shedding patterns. The data show a trail of shear layer vortices, forming a weakly mixed Kármán street along the foil path, with strong LE separation. The data for Case 1(a) show similar patterns. From the wake momentum, it is also not evident that strong thrust is produced.

In Anderson's experiments for the 2D foil, she characterized the wake pattern in region B as one comprising of a Kármán street with a sluggishly organized LE vortex (Region B). The vorticity plots for case 1 show agreement with her observations. Although the flow parameters for the lower half of the foil, at 0.8S from the root (Cases 1(b) and 2(b)), fall in Region C (jet wake formation), the vortex pattern seen at 0.5S (Cases 1(a) and 2(a)), which is a less organized shedding of vorticity, dominates along the span instead.

Cases 1 and 2 were compared to see whether there was an effect of increasing $\alpha_{\max}$. At the higher angle of attack (Case 2), the LE separation appears to be more pronounced. The LE vortex is seen rolling up along the foil and shedding from the TE just as the foil is about to change direction at zero pitch angle. As Strouhal number increases from 0.2 to 0.5, the vortex shedding is observed to be more energized with distinct vortices being shed in the wake. The vortical signature is predominantly similar to what is expected in region C, although this is not easily discernible from the limited field of view in the PIV images. It is good to note here that the field of view covers only up to ±5 deg roll, compared with the maximum roll amplitude of ±10.3 and ±13.7 deg at each spanwise position visualized.

For cases 3 and 4 there is little evidence of the paired vortex arrangement, except for case 4(b), which falls in Anderson's D region. Considering the linear taper of the foil, it is noted that the main upper portion of the foil, by virtue of geometry, falls within Region C, while only the lower quarter (0.7S and beyond) falls in Region D based on its equivalent two-dimensional flow parameters. By material continuity and slow changes in geometry, the conventional jet-like wake pattern of region C overwhelms the wake region. It is less likely for the vortex formation along the span to have two distinct shedding patterns as the foil taper is very slight and the foil span is relatively small.

PIV results from case 3 show a reverse Kármán street wake. Figure 13 (a) and (b) show the vorticity from case 3(a) and 3(b), respectively, at two distinct phases of roll and pitch motion. In these plots red represents clockwise circulation and blue is counter-clockwise circulation. Due to the limited field of view and the speed of the motion and fluid flow, both the right and left-moving strokes are necessary to visualize the complete wake. On each stroke one vortex is shed into the wake. As the foil traverses through its roll cycle, the leading edge vortex is strengthened and finally shed at the extreme roll position before the foil returns in the opposite direction. The vortices shed at each extreme are counter-rotating such that they form a jet-like wake. This pattern corresponds with the C-region in the Anderson plot (figure 12).

A mixed vortex pair is observed at the 0.8S, for case 4(b). A close look at the velocity vector plot (see figure 14) shows a strong jet-like structure being produced at an oblique angle to the flow direction per half cycle of motion. It is interesting to note that this case yielded good values of C_T and η. From basic momentum analysis, the existence

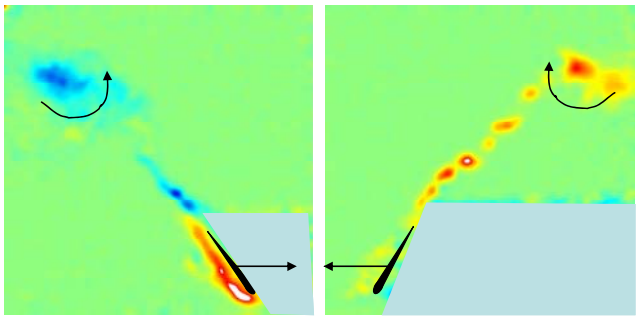

a) Case 3(a)

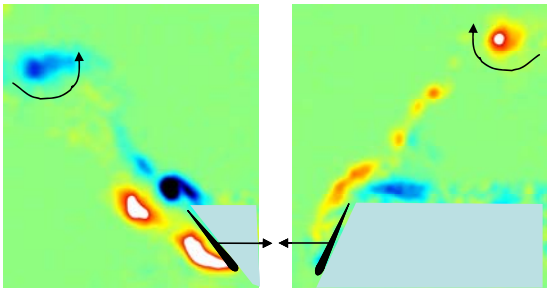

b) Case 3(b)

Figure 13: Phase averaged PIV results for case 3. The upper images show the plane taken at the 0.5 span point (cut A) and the lower two images are taken at cut B. The left images show the counterclockwise vorticity shed from the foil as it moves from left to right and the images on the right show the clockwise rotating vortex shed as the foil traverses in the opposite direction (right to left). This shedding of alternate signed vortices for each half cycle combines to generate the thrust wake behind the foil as expected.

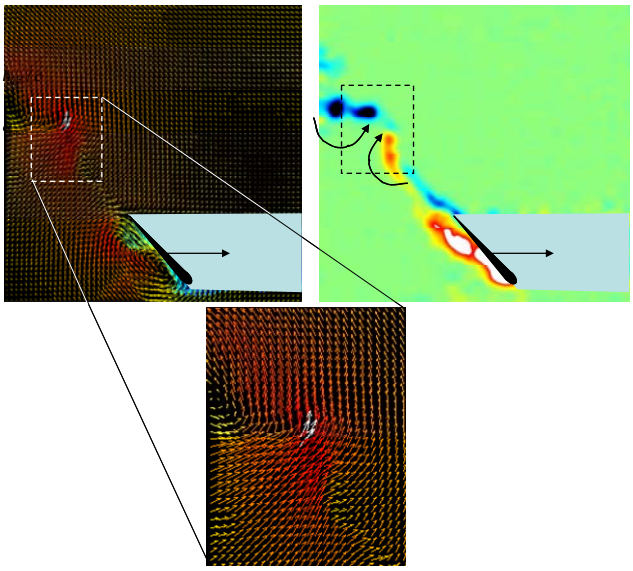

Figure 14: Phase averaged PIV results for case 4(b). As the foil traverses from one side to the other, it sheds two counter rotating vortices per half cycle. The left image shows the overall vector field and the right image the vorticity, the arrows indicate the direction of rotation. A close-up of the vectors in the vicinity of the vortex pair is shown in the inset.

of this velocity jet in the wake gives rise to thrust. Kinetic energy being imparted to the flow naturally translates to power losses. However, the large thrust force produced by the large roll motion does seem to recover some of the loss with high efficiencies being recorded.

Figure 14 shows the velocity vector and vorticity plots at only one phase. The vortex pattern is slightly different from the case presented by Anderson in Region D. Here the jet formed by the vortex pair is angled inwards toward the centerline and aft. In Anderson's case, it was angled outward and aft. A possible reason for the difference is the fact that Anderson used a different motion profile for this case. While pure sinusoids for pitch and roll are used in our case, she employed a double peak square wave motion profile for pitch.

Since results from 4(a) show a more standard jet wake pattern, it is unclear from these tests whether or not the pattern for slice 4(b) is due to the tip vortex rolling upwards and interacting with the TE vortex or simply a mixed vortex pair as expected in region D. The limited field data, and lack of 3D visualization, collected renders it difficult to determine whether this vortex pair is indeed composed of both LE and TE vortices versus a pairing up of the tip vortex with the TE vortex. Nevertheless, the plots seem to suggest highly three-dimensional effects and more detailed investigation of this tip region is necessary to fully understand the wake structure beyond 0.7S.

5. CONCLUDING REMARKS

Force and efficiency measurements were conducted using the MC1 six-axis sensor for over a range of flow parameters. The sensor proved to be reliable, with force measurements in agreement with those from the tunnel dynamometer (within the useful calibrated range). The

results showed a dependency of thrust and efficiency with *St* and α_{max} values, similar to that obtained by Read, as well as [17], for the two- and three-dimensional cases respectively. For a given Strouhal number, there is a critical α_{max} value beyond which the thrust coefficient will start to decrease. A peak planform area thrust coefficient of 2.09 was measured at $h_{0.7}/c$ = 1.5, *St* = 0.6 and α_{max} = 30º. Increasing the heave to chord ratio from 1.5 to 2.0 does not appear to improve C_T values. It appears that somewhere between this range is an optimal $h_{0.7}/c$ value for which maximum thrust production can be achieved.

Hydrodynamic efficiency ranged from 0.14 to 0.8. It is noted that for low α_{max} values, thrust generally increases with Strouhal number, without much penalty to efficiency. This would be of much interest to power systems design as an optimal point can be identified for relatively high thrust production with good efficiencies.

Combined with data from [17], the data obtained here suggests a useful performance trend where at low α_{max}, high thrust and high efficiency can be gained at sufficiently high Strouhal numbers (St = 0.6 and possibly higher). In particular, at higher roll amplitudes, the large oscillations produce large thrust with relatively less power loss. It is good to note, also, that for the case of a 2D foil higher thrust and efficiencies can be achieved through preshaping algorithms applied to the foil motion [10]. It is estimated that similar preshaping could improve the performance of the 3D foil as well. Of course, further investigations are needed to confirm this.

The percentage errors associated with the measurements remain significant at the low thrust regimes. Overall, the test runs display good repeatability. The error margins obtained show that the six-axes sensor is able to provide reasonable resolution at the force range measured (0 ~10N). It is noted that the range of measurements taken was up to 10% of the sensor's capacity. To drive percentage errors down, it would be advantageous to operate at higher force ranges. This would mean utilizing higher flow velocities and scaling the flapping frequencies higher to obtain the same flow parameters.

DPIV tests on four flapping cases, at two planes of view, showed the flow signature over both low and high thrust regimes. The effect of Strouhal number and roll amplitudes led to varying vortical signatures ranging from weakly mixed Kármán streets to thrust-producing jet-wakes and mixed vortex shedding patterns. The effect of increasing the angle of attack is less dramatic, with LE separation becoming more pronounced.

The mixed vortex pair is observed for the case where efficiency and thrust measurements were relatively high. This mixed vortex pattern is somewhat different from that observed by [2], [4] for the two-dimensional flapping foil. It is interesting to note that where the mixed pairing occurred, the case yielded high thrust and efficiency values. Further study is needed to determine the whole three-dimensional structure of the wake that could result in optimal propulsor performance.

ACKNOWLEDGEMENTS—The authors would like to acknowledge the support of Admiral Paul Sullivan, through NAVSEA, in addition to ONR, NOAA and MIT Sea Grant (Grant NA 16RG2255).

REFERENCES

[1] Adrian, R.J., 1991, "Particle-imaging techniques for experimental fluid mechanics", *Ann. Rev. Fluid Mech*., 23, 261-302.

[2] Anderson J. M., 1996, "Vorticity control for efficient propulsion", *PhD thesis*, MIT/Woods Hole Oceanographic Institution.

[3] Anderson, J.M., & Chabra, N., 2002, "Maneuvering and stability performance of a robotoic tuna," *Integrative and Comp. Bio.* 42(1): 118-126.

[4] Anderson, J.M., Streitlien, K., Barrett, D.S., & Triantafyllou, M., 1998, "Oscillating foils of high efficiency", *J. Fluid Mech*., 360, 41-72.

[5] Bandyopadhyay P.R., J.M. Castano, J.Q. Rice, R.B. Philips, W.H. Nedderman & W.K. Macy, 1997, "Low speed maneuvering hydrodynamics of fish and small underwater vehicles", *J. Fluids Engin.*, 119, 136-119.

[6] Fish F.E., 1997, "Biological designs for enhanced maneuverability: Analysis of marine mammal performance", *10th Int. Symp. Unmanned Untethered Submersible Technology*, Special Session on Bio-Engineering Research Related to AUV, Durham, NH, pp. 109-117.

[7] Fish F.E., & Hui C.A., 1991, "Dolphin swimming - a review", *Mammal Rev.*, 21, 181-95.

[8] Flores M.D., 2003, "Flapping motion of a three-dimensional foil for propulsion and maneuvering of underwater vehicles", *Masters thesis*, MIT/Ocean Engineering.

[9] Freymuth P., 1988, "Propulsive vortical signature of plunging and pitching airfoils", *AIAA J*., 26, 881-883.

[10] Hover, F.S., Haugsdal, O, & Triantafyllou, M.S., 2004, "Effect of angle of attack profiles in flapping foil propulsion," *J. Fluids and Structures*, vol. 19, pp. 37-47.

[11] Kato N., 2000, "Control performance of fish robot with mechanical pectoral fins in horizontal plane", *IEEE J. Oceanic Engineering*, 25 (1), 121-129.

[12] Kemp, M., Hobson, B. & Pell, C., 2003, "Energetics of the oscillating fin thruster", *Proc. 13th Intern. Symposium on Unmanned Untethered Submersible Technology (UUST)*, Durham New Hampshire.

[13] Koochesfahani, M., 1989, "Vortical Patterns in the Wake of an Oscillating Foil," *AIAA J*., 27, pp. 1200–1205.
[14] Lauder G.V., 2000, "Function of the caudal fin during locomotion in fishes: Kinematics, flow visualization and evolutionary patterns", *Amer. Zool.*, bf 40, 101-122.
[15] Lim, K. L., 2005, "Hydrodynamic Performance and Vortex Shedding of a Biologically Inspired Three-Dimensional Flapping Foil," *Masters Thesis*, MIT Ocean Engineering.
[16] McCroskey W.J., 1982, "Unsteady airfoils", *Ann. Rev. Fluid Mech*., 14, 285-311.
[17] McLetchie, K., 2004, "Forces and hydrodynamic efficiency measurements of a three dimensional flapping foil", *Masters Thesis*, MIT/Ocean Engineering.
[18] Miklosovic, D.S., Murray, M.M., Howle, L.E., & Fish, F.E. 2004, "Leading-edge tubercles delay stall on humpback whale (*Megaptera novaeangliea*) flippers," *Physics of Fluids*, 16(5): 39:42.
[19] Mueller U., B. van den Heuvel, E. Stamhuis & J. Videler, 1997, "Fish foot prints: Morphology and energetics of the wake behind a continuously swimming mullet (*Chelon Labrosus Risso*)", *J. Exp. Biol.*, 200, 2893-2806.
[20] Polidoro, V., 2003, "Flapping foil propulsion for cruising and hovering autonomous underwater vehicles", *Masters Thesis*, MIT/Ocean Engineering.
[21] Read D., 2000, "Oscillating foils for propulsion and maneuvering of ships and underwater vehicles", *Masters thesis*, MIT/Ocean Engineering.
[22] Read D.A., Hover F.S., & Triantafyllou M.S., 2003, "Forces on oscillating foils for propulsion and maneuvering", *J. Fluids and Struct*., 17, 163-183.
[23] Stamhuis E., & J. Videler, 1995, "Quantitative flow analysis around aquatic animals using laser sheet particle image velocimetry", *J. Exp. Biol.*, 198, 283-94.
[24] Triantafyllou, M.S., A. H. Techet, and F.S. Hover, "Review of Experimental Work in Biomimetic Foils," IEEE Journal of Oceanic Engineering, v. 29(3), pp. 585-594, 2004.
[25] Triantafyllou, M. S., F.S. Hover, A. H. Techet and D. K. P. Yue, 2005, "Review of Hydrodynamic Scaling Laws in Aquatic Locomotion and Fishlike Swimming," *Appl. Mech. Review*, vol. 58.
[26] Triantafyllou, M. S., Triantafyllou, G. S., and Gopalkrishnan, R., 1991, "Wake Mechanics for thrust Generation in Oscillating Foils," *Phys. Fluids*, 3(12), pp. 2835–2837.
[27] Triantafyllou G.S., Triantafyllou M.S., & Grosenbaugh R., 1993, "Optimal thrust development in oscillating foils with application to fish propulsion', *J. Fluids and Struct*., 7, 205–224.
[28] Triantafyllou, M. S., Triantafyllou, G. S., and Yue, D. K. P., 2000, "Hydrodynamics of Fish Swimming," *Ann. Rev. Fluid Mech*., 32, pp. 33-53.
[29] Videler J., 1993, *Fish Swimming*, London: Chapman and Hall.
[30] Willert, C.E., & Gharib, M., 1991, "Digital particle image velocimetry", *Exp. Fluids*, 10, 181-193.
[31] Wolfgang M.J., J.M. Anderson, M.A. Grosenbaugh, D.K.P. Yue, & M.S. Triantafyllou, 1999, "Near-body flow dynamics in swimming fish", *J. Exp. Biol.*, 202, 2303-2327.